



# P25 titanium dioxide coated magnetic particles: Preparation, characterization and photocatalytic activity



Roghi E. Kalan<sup>a,b</sup>, Sudheera Yaparathne<sup>b,c</sup>, Aria Amirbahman<sup>a,b,c</sup>, Carl P. Tripp<sup>a,b,\*</sup>

<sup>a</sup> Laboratory of Surface Science and Technology, (LASST), University of Maine, Orono, ME, USA

<sup>b</sup> Department of Chemistry, University of Maine, Orono, ME, USA

<sup>c</sup> Department of Civil and Environmental Engineering, University of Maine, Orono, ME, USA

## ARTICLE INFO

### Article history:

Received 16 July 2015

Received in revised form 7 December 2015

Accepted 8 January 2016

Available online 13 January 2016

### Keywords:

P25 TiO<sub>2</sub>

Magnetic particles

Photocatalyst characterization

Water purification

## ABSTRACT

The photocatalytic properties of magnetic iron(II,III) oxide particles coated with different wt% of commercially available P25 TiO<sub>2</sub> (P25) using a simple wet impregnation method were measured. The produced materials were characterized by XRD, XPS, SEM, TEM, EDX, FTIR, ICP, Magnetic Property Measurement System (MPMS) and BET (N<sub>2</sub>). After calcination at 500 °C of the magnetic particles that was loaded only with P25, the P25 was strongly bound through a redox reaction with the magnetic particles. It was found that the P25 surface coverage was almost complete (>95%) at a 1:1 mass loading ratio; at higher P25 mass ratios, a thicker coating was obtained. However, the photocatalytic degradation rates of terephthalic acid (TPA) and phenol for these particles at all P25 loadings was lower than those obtained for pure P25 on a per TiO<sub>2</sub> mass basis. Precoating the magnetic particles with a SiO<sub>2</sub> sol-gel layer prevented the electron hole migration and oxidation of magnetite to hematite, but also led to a weakly bound P25 layer that was removed by rinsing. This was overcome by adding a second TiO<sub>2</sub> sol-gel on top of the SiO<sub>2</sub> coated magnetic particles coating for anchoring the P25 particles to the surface. While magnetic particles consisting of a silica undercoat followed by a TiO<sub>2</sub> sol-gel coating as the photocatalytic layer have been reported, our approach is to use the TiO<sub>2</sub> sol-gel coating as an adhesion layer to anchor P25 particles. The P25 adhered strongly to this underlying TiO<sub>2</sub> sol-gel layer without significant loss of surface area. In both P25 and our produced photocatalyst, during the photocatalytic reaction P25 is in direct contact with water and the process occurs on the P25 and water interface. As a result, the photocatalytic degradation rates of TPA and phenol by the P2- coated magnetic particles were found to be equivalent to those of P25. The pseudo-first order rate constants in the P25 mass basis for photocatalytic degradation of TPA were  $0.0152 \pm 0.003 \text{ min}^{-1}$  and  $0.0144 \pm 0.007 \text{ min}^{-1}$  using pure P25 and SiO<sub>2</sub> sol-gel/TiO<sub>2</sub> sol-gel/P25 coated magnetic particles, respectively. The rate constant for phenol photocatalytic degradation was reported  $0.09 \pm 0.02 \text{ min}^{-1}$  for pure P25 and  $0.10 \pm 0.04 \text{ min}^{-1}$  for SiO<sub>2</sub> sol-gel/TiO<sub>2</sub> sol-gel/P25 coated magnetic particles. The similar specific surface area of the P25 powder and the P25 anchored to the surface in SiO<sub>2</sub> sol-gel/TiO<sub>2</sub> sol-gel/P25 coated magnetic particles is the reason for these similarity for rate constants.

© 2016 Elsevier B.V. All rights reserved.

## 1. Introduction

Direct ultraviolet (UV) radiation as a means for treatment of drinking water has gained interest in recent years among water treatment plants that use surface waters as the source. As of 2007, 2% of the drinking water treatment facilities in the USA used UV illumination; since then, this number has increased and is expected to increase significantly in the coming decades due to UV's effectiveness in inactivating protozoa and its lack of production of treatment

byproducts [1]. However, direct UV photolysis is not as effective for the removal of most emerging contaminants in water, such as algal toxins, pharmaceutical and personal care products (PCCPs), or for the inactivation of most viruses [1–3]. UV illumination of photocatalysts leads to the generation of highly reactive hydroxyl radicals (HO•) that destroy organic pollutants [4], while also inactivating certain water-borne viruses. The photocatalyst efficiency of HO• depends on many parameters such as solution pH, concentration of catalyst, light intensity and wavelength, and pollutant concentration [5].

Among the semiconductor metal oxide nanoparticles, commercially available P25 titanium dioxide with the particle size of 20–30 nm is generally accepted as the “gold standard” photocatalyst for water treatment [6]. P25 is a mixture of anatase and rutile

\* Corresponding author at: Laboratory of Surface Science and Technology, (LASST), University of Maine, Orono, Maine, USA.

E-mail address: [ctripp@maine.edu](mailto:ctripp@maine.edu) (C.P. Tripp).

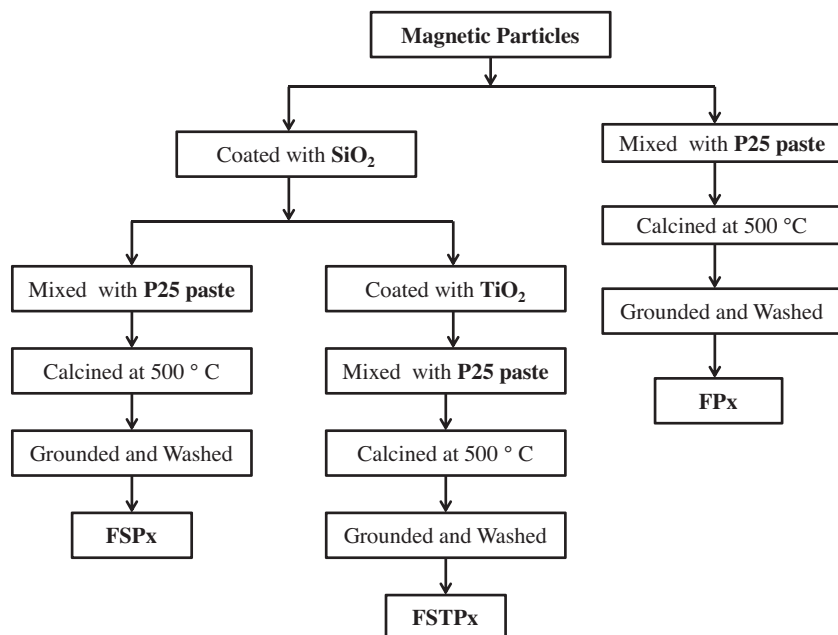


Fig. 1. Flow chart for preparation of the coated magnetic particles.

with band gap energies of 3.2 eV and 3.0 eV, respectively [7–11]. A critical issue in using P25 suspensions arises from the difficulty in removing the P25 from a suspension; separation and recovery of the P25 with a conventional filtration method is time consuming and economically not practical. One approach to overcome this hurdle is to immobilize a  $\text{TiO}_2$  sol-gel layer on different substrates such as glass, stainless steel, silica, clay [12–14], and magnetic particles [8,15–18]. For the latter, a particular attraction of using coated magnetic particles is that they could be introduced to the water supply upstream from the UV treatment subsystem and captured downstream with a magnet. The  $\text{TiO}_2$ -coated magnetic particles would then be recycled back upstream of the UV system [19].

When using magnetic particles such as magnetite ( $\text{Fe}_3\text{O}_4$ ), the common approach is to apply a  $\text{SiO}_2$  undercoat before applying a  $\text{TiO}_2$  layer [20,21]. This is because the direct contact of  $\text{TiO}_2$  with the iron oxide core leads to lower photocatalytic activity. The conduction band in the iron oxide is lower in energy than  $\text{TiO}_2$  and thus, the photo-generated holes in the  $\text{TiO}_2$  layer readily migrate into the iron oxide lattice resulting in lower radical production levels at the  $\text{TiO}_2$ /water interface. Furthermore, iron oxide has a narrow band gap and electron-hole recombination occurs readily in this material [7,22,23]. Electron transfer from the  $\text{TiO}_2$  conduction band into the iron oxide core results in the reductive dissolution of  $\text{Fe(III)}$  [21,22]. The  $\text{SiO}_2$  undercoat overcomes this problem by providing an insulative layer between the iron oxide from the  $\text{TiO}_2$ . The  $\text{SiO}_2$  layer has the added advantage of acting as a hole trapping layer preventing electron-hole recombination in the  $\text{TiO}_2$  structure [8,15,18,24,25]. While there is an improvement in photocatalytic degradation using a  $\text{SiO}_2$  barrier, these materials still exhibit lower catalytic activity than P25. These lower activities are reported to be because of a lower surface area or hole migration to the core due to partial  $\text{SiO}_2$  coverage [26–28].

The formation and use of a  $\text{TiO}_2$ -coating on top of the silica barrier layer to degrade organic compounds in water has been the subject of several studies [7,16,21,27,29–32]. In all cases, both the  $\text{SiO}_2$  and  $\text{TiO}_2$  layers are deposited using sol-gel methods that produce an amorphous  $\text{TiO}_2$  coating which when upon calcination at an elevated temperature is converted to anatase or rutile. Generally, the thickness of the  $\text{TiO}_2$  layer synthesized on the magnetic particles surface is in the range of 5–10 nm [16,17,22,33,34]. How-

ever, in most cases, the photocatalytic degradation rates of organic compounds by these photocatalysts are lower compared to that of P25 [26–28]. An alternative approach to synthesis using a sol-gel  $\text{TiO}_2$  layer is to directly coat the magnetic core with a layer of P25 particles. Typically the P25 is added to sol-gel formulation containing a  $\text{TiO}_2$  precursor or is blended with iron oxide particles or  $\text{SiO}_2$  coated iron oxides [19,26,27]. The material is then calcined at an elevated temperature to sinter the P25 to the magnetic particles. This approach is attractive due to its simplicity. This study focuses on the photocatalytic performance and material optimization of P25-coated magnetic particles. More important, there have been no examples reported where P25-coated magnetic particles have shown to have equal or better photocatalytic degradation rates compared to pure P25. However, direct comparison of photocatalytic activities is difficult, since factors such as the photocatalyst concentration and the adsorption of the compound onto the catalyst could be different [7,35,36]. For example, increasing photocatalyst concentration increase the photocatalytic degradation rate, but it can also increase the opacity of the suspension and cause scattering of the UV light [35]. As a result, the basis for reported comparisons are often empirical in nature or not stated.

When coating magnetic particles with a P25/ $\text{TiO}_2$  sol-gel matrix [19], the coatings most likely have a portion of the P25 encased in the  $\text{TiO}_2$  sol-gel matrix and not directly in contact with water. In our work, a thin  $\text{TiO}_2$  sol-gel film was first deposited on top of the silica-coated magnetic particles followed by deposition of P25 in a separate step. Upon heating at 500 °C, the P25 is anchored to the underlying  $\text{TiO}_2$  sol-gel film via formation of Ti–O–Ti bonds. This led to a P25 layer that effectively had no reduction in effective surface area in contact with the water and resulted in photocatalytic degradation levels for terephthalic acid (TPA) and phenol which were equivalent to the P25 on a P25 mass basis. While both a silica and  $\text{TiO}_2$  sol-gel coating were required, the  $\text{TiO}_2$  sol-gel coating in our approach was not used as the photocatalytic layer but rather as an adhesion layer [12,37–40] for anchoring the P25 particulates. We used TPA and phenol in this study because they are common standard probes for measuring photocatalytic activities [41,42]. Further, TPA is commonly used to characterize  $\text{HO}^\bullet$  production [43].

## 2. Experimental

### 2.1. Chemicals

The magnetite particles ( $\text{Fe}_3\text{O}_4$ , iron(III, II) oxide, 50–100 nm, 97% trace metals basis) were obtained from Aldrich, and the P25  $\text{TiO}_2$  powder was obtained from Evonik (formerly Degussa). Anhydrous ethanol (200 proof), 2-propanol (99.99%), aqueous ammonia (wt% 28.0–30.0  $\text{NH}_3$  basis), tetraorthosilicate (TEOS, 99.99%), titanium(IV) isopropoxide (99.99%), terephthalic acid (TPA, 98%), phenol (99%), and 2-hydroxyterephthalic acid (hTPA, 97%) were purchased from Sigma Aldrich. Deionized water (DI, 18 M $\Omega$ cm) was obtained from a Millipore gradient A10 water purification system. Nitrocellulose membranes of 0.45 and 0.22  $\mu\text{m}$  pore size were obtained from Millipore.

### 2.2. Synthesis of photocatalysts

P25-coated magnetic particles were prepared using three different pathways as described in Fig. 1. Photos of samples produced at various steps along the preparative pathway are provided in the SI section (Fig. S1).

#### 2.2.1. $\text{SiO}_2$ -coated magnetic particles (FS)

Magnetic particles were coated with a  $\text{SiO}_2$  layer using a sol-gel method described elsewhere [8]. In brief, a 1.00 g sample of magnetic particles was dispersed into a solution containing 400 ml of ethanol, 100 ml of DI water and 12 ml of ammonia. The suspension was ultrasonicated for 30 min and then transferred to a 1 l beaker. TEOS (3.5 ml) was then added drop-wise over a period of a minimum of 15 min, while vigorously stirring at 500 rpm, and the suspension was stirred for an additional 5 h. The particles were removed from the suspension by placing a magnet on the side of the beaker and decanting the solution phase. The particles were then rinsed with DI water several times and dried in the vacuum oven at 50 °C for 2 h.

#### 2.2.2. Sol-gel $\text{TiO}_2$ - and $\text{SiO}_2$ -coated magnetic particles (FST)

$\text{SiO}_2$ -coated magnetic particles were coated with  $\text{TiO}_2$  using a sol-gel method reported elsewhere [8,30]. A 0.50 g sample of the FS particles was dispersed in 80 ml of ethanol and stirred at 500 rpm for 10 min. Then, a freshly prepared solution of 2.4 ml of titanium(IV) isopropoxide in 16 ml ethanol was added drop-wise (minimum of 15 min) to the particulate suspension at 70 °C while vigorously stirring at 500 rpm. The suspension was then stirred for an additional 12 h. The particles were removed from the suspension by placing a magnet on the side of the beaker and decanting the solution phase. These particles were then rinsed with DI water several times and dried in the vacuum oven at 60 °C for 2 h. The dried particles were heated in air to 500 °C at a rate of 5 °C min<sup>-1</sup>, held at this temperature for 5 h, and then cooled down to room temperature at a rate of 5 °C min<sup>-1</sup>.

#### 2.2.3. P25-coated magnetic particles (FPx, FSP and FSTPx)

A thick paste was prepared by adding 0.4 ml DI water to 0.50 g of P25. The paste was mixed thoroughly using a spatula to produce a uniform mixture (Fig. S1a). Three types of particles were prepared by adding bare magnetic particles (FPx), FS particles (FSP), or FST particles (FSTPx) to the P25 paste (Fig. S1b). The pastes were then mixed thoroughly using a spatula to produce a homogeneous mixture. The amounts of magnetic particle added to the paste are given in Table 1. Table 1 also provides the sample labeling system used in this manuscript. The paste was then heated in air to 500 °C at a rate of 5 °C min<sup>-1</sup>, held at 500 °C for 5 h, followed by cooling to room temperature at a rate of 5 °C min<sup>-1</sup> (Fig. S1c). Samples were then ground (Fig. S1d) in a mortar and pestle and size selected (<150  $\mu\text{m}$ )

**Table 1**

Amounts used in preparation of each material. F, S, T and P, refer to iron oxide, sol-gel grown  $\text{SiO}_2$  layer, sol-gel grown  $\text{TiO}_2$  layer, and P25, respectively. The numbers refer to the mass ratio of the iron oxide and P25 in each sample.

Samples	P25 (g)	Magnetic particles (g)	TEOS (ml)	Titanium(IV) Isopropoxide (ml)
FP1	0.500	0.500	0	0
FP2	0.500	0.250	0	0
FP3	0.500	0.167	0	0
FP4	0.500	0.125	0	0
FP5	0.500	0.100	0	0
FSP2	0.500	0.250	2.6	0
FSTP1	0.250	0.250	2.6	2.4
FSTP2	0.500	0.250	2.6	2.4

by passing the particles through a Cole-Palmer sieve shaker. The powders were rinsed with DI water and removed from the suspension by placing a magnet on the side of the beaker and decanting the solution phase. The particles were then dried at 80 °C for 1 h.

### 2.3. Particle characterization

Powder X-ray diffraction (XRD) patterns of particles were obtained on a PANalytical X'pert MRD X-ray diffraction system using Cu-K $\alpha$  radiation at a scan rate of 0.3° s<sup>-1</sup>. X-ray photoelectron spectroscopy (XPS) was obtained on a dual anode VG Microtech X-ray source and a SPECS HSA2000 analyzer. Scanning electron microscopy (SEM) and energy dispersive X-ray spectroscopy (EDX) were measured on a Zeiss N vision 40 system. The particles morphology and size distribution were examined by transmission electron microscopy (TEM) on a Philips CM10, 100kv, camera controller Orius, CCD. The BET surface area was determined by a multipoint method on a Micromeritics ASAP 2020 using the adsorption data in the relative pressure range (P/P0) of 0.02–0.45. The elemental composition was obtained by digesting the samples in a solution containing equal volumes of HF(5%), HCl(6M), and HNO<sub>3</sub>(7.5 M). The digested samples were analyzed using a Thermo Element2 sector field Inductively Coupled Plasma Mass Spectrometer (ICPMS). FTIR spectra were recorded on ABB FTLA 2000 spectrometers. Magnetic properties were measured using a Magnetic Property Measurement System (MPMS XL; Quantum Design, Inc.) at 300 K and magnetic fields of 0 to  $\pm 70$  kOe, and the data was analyzed using Igor Pro. The fluorescence spectra were recorded on a Jobin Yvon Fluorolog-3 spectrofluorometer equipped with emission and excitation monochromators, a 400 W Xenon lamp source, and a photomultiplier tube. High Performance Liquid Chromatography (HPLC) analysis of phenol and TPA concentrations were performed on an Agilent 1100 with a C8 column (100A).

### 2.4. Photocatalytic degradation experiments

Photocatalytic activities of the coated magnetic particles were measured using TPA as a probe molecule for HO $\cdot$  production. The reaction product of TPA with HO $\cdot$  is hTPA whose fluorescence intensity is proportional to the HO $\cdot$  concentration [43]. A 0.075 g sample of the magnetic particles was dispersed in 50 ml DI water in a 250 ml quartz beaker and sonicated for 1 min. The particles in the suspension were then collected by placing a magnet at the bottom side of the beaker and decanting the solution phase. Next, 150 ml of a 83 mg/L TPA solution was added to the beaker containing the magnetic particles. The pH was in the 6.0–6.4 range after the addition of the catalysts and remained in this range over the entire experiment. The beaker was then placed in the photochemical chamber of a Rayonet Model RPR-100 reactor that was equipped with four RPR-2537 Å lamps, each emitting radiation in the UV-C range ( $\sim 254$  nm) of  $1.26 \times 10^{-5}$  einstein min<sup>-1</sup> (15.6 W m<sup>-2</sup>), measured by the ferrioxalate actinometry method [44,45]. A 254 nm lamp was selected

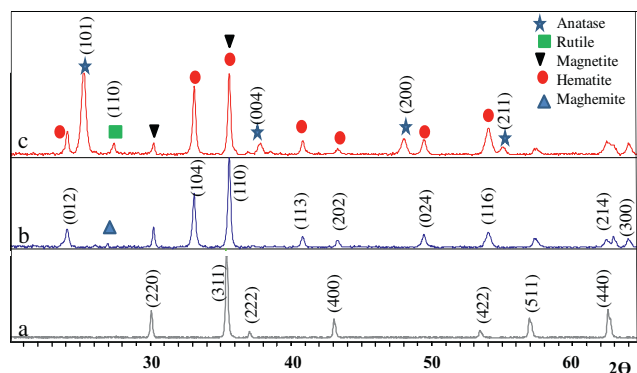


**Fig. 2.** XRD patterns for (a) magnetite (b) calcined bare magnetite particles, and (c) FP1. (For interpretation of the references to color in the text, the reader is referred to the web version of this article.)

in our experiments, as this is the same wavelength used in low pressure Hg UV lamps in water treatment plants. The suspension was stirred at 100 rpm using a home-built overhead glass rod propeller. After stirring in the dark for a minimum of 15 min, a sample was withdrawn to measure the dark adsorption of TPA onto each catalyst. Then, at specified intervals during illumination, 3 ml aliquots of the stirred suspension were withdrawn using a 10 ml syringe equipped with a 30 cm long plastic tube. The total volume extracted from the starting 150 ml in any given experiment was less than 20 ml. Each 3 ml sample was passed through a 0.45  $\mu\text{m}$  pore size filter to remove the magnetic particles. One ml of the filtered sample was transferred to a 20 ml volumetric flask and diluted with DI water. To measure the hTPA concentration, a portion of this diluted sample was transferred to a standard 1 cm cuvette and the fluorescence spectra were measured over the range of 350–500 nm. The excitation frequency was set at 315 nm with a side entrance and exit slit of 3 nm with 0.5 s integration time. TPA concentrations were measured using HPLC at 238 nm with a mobile phase of acetonitrile (40% v/v) and water (60% v/v). All experiments were repeated a minimum of three times.

For measuring the photocatalytic degradation of phenol, 0.075 g of the magnetic particles was added to 150 ml of 10 mg/L phenol (pH,  $6.0 \pm 0.2$ ). The suspension was stirred in the dark for a minimum of 15 min prior to the start of UV illumination and a sample was withdrawn to measure the dark adsorption of phenol. The same experimental protocol used for extracting TPA samples for analysis was also used in the measurement of phenol. The phenol concentration in solution after filtration was analyzed using HPLC with mobile phase acetonitrile (20% v/v) and water (80% v/v) at 254 nm wavelength.

### 2.5. Photodissolution experiments

For photodissolution experiment, after completion of the TPA photocatalytic degradation experiments, the suspensions with pH of 6.0–6.4 were kept in the dark without stirring for 30 min to allow particle sedimentation. Then, a 10 ml aliquot of supernatant was passed through a 0.22  $\mu\text{m}$  pore size nitrocellulose membrane to remove any residual particles. The filtered samples were analyzed for Fe, Ti and Si using the ICPMS.

## 3. Results and discussion

### 3.1. X-ray diffraction studies

The XRD patterns for the bare magnetic particles before and after calcination, along with the sample FP1, are shown in Fig. 2. All peaks for the magnetic particles before calcination (Fig. 2a) are assigned

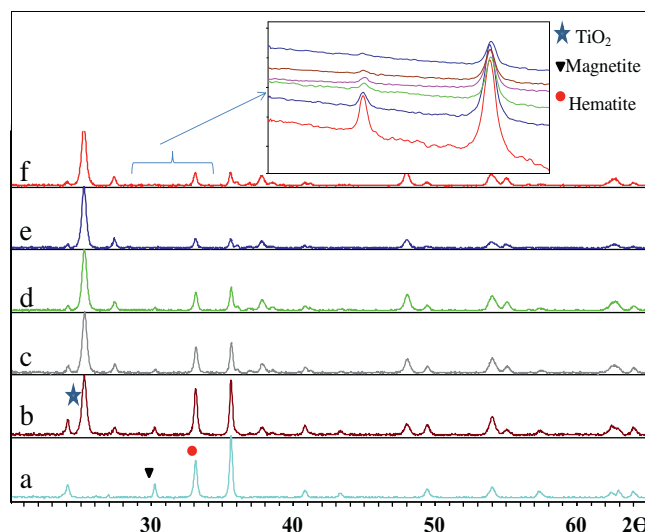


**Fig. 3.** XRD pattern of (a) calcined magnetite (b) FP1, (c) FP2, (d) FP3, (e) FP4, and (f) FP5.

to magnetite according to the International Centre for Diffraction Data, Powder Diffraction File (ICCD, PDF 01-080-6402). A common step in the generation of all P25-treated materials is calcination at 500 °C. Thus, for comparative purposes, the XRD pattern for the bare magnetic particles that have undergone the calcination protocol used in this work is provided in Fig. 2b. In Fig. 2b, peaks are assigned to magnetite and hematite (ICCD, PDF 01-080-2377) and a trace of maghemite. Calcination of the bare magnetic particles leads to oxidation of magnetite to hematite, resulting in particles composed of a mixture of magnetite and hematite. This calcination step also leads to a color change from black to reddish brown.

In the XRD pattern for FP1 (Fig. 2c), peaks for magnetite, hematite, and P25 are obtained. As found with the bare magnetic particles calcined in air, calcination of FP1 samples also leads to the conversion of the magnetite to hematite. Peaks at 30.02° and 33.12° are unique to magnetite and hematite, respectively, and thus, the intensity of these two peaks can be used to monitor the relative amount of each compound in the particles. For example, the peak intensity ratio of 30.02°:33.12° for FP1 (Fig. 2c) is higher than the corresponding ratio for the calcined bare magnetic particles (Fig. 2b), showing that the P25 coating leads to a higher level of oxidation of the magnetic particles than the O<sub>2</sub> in the air. In addition, the redox reaction between the magnetic particles and P25 suggests that P25 must be in intimate contact with the magnetic particles. Reduction of P25 is further supported by the change in color of the particles from black to reddish brown [46]. This color change is not due to diffusion of iron from the core to the P25. XPS and EDX analysis shows that iron is not located at the surface of the P25 particles (see Section 3.3).

The XRD patterns for various FPx samples are shown in Fig. 3. The inset shows that the 30.02°:33.12° peak ratio decreases with higher P25 loading. Thus, there is an increase in the extent of oxidation of magnetite to hematite with an increase in P25 loading. To obtain an estimate of the extent of oxidation of magnetite to hematite, we used the 30.02°:35.6° and 33.12°:35.6° peak ratios (Fig. S2). The peak at 35.6° is a combination of the (3 1 1) and (1 1 0) peaks of magnetite and hematite, respectively (Fig. 2). Given the similar bulk density for these two iron oxides (hematite, 5.2 g cm<sup>-3</sup> and magnetite 5.0 g cm<sup>-3</sup>), this peak provides a reasonable estimate of the total iron oxide. The 30.02°:35.6° peak ratios for 100% magnetite (ICCD, PDF 01-080-6402) has a value of 0.3 and the corresponding 33.12°:35.6° peak ratio for 100% hematite (ICCD, PDF

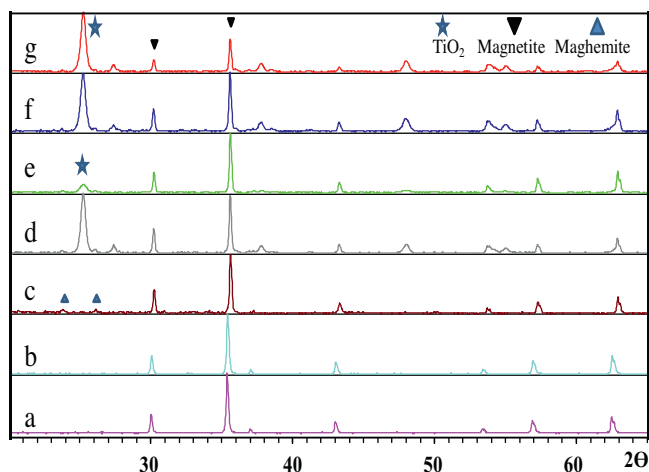


**Fig. 4.** XRD patterns for (a) magnetite (b) FS, (c) FS calcined, (d) FSP2, (e) FST, (f) FSTP1, and (g) FSTP2.

01-080-2377) was 1.4. These values were used to convert the peak ratio in the various samples to % composition. Fig. S2 shows FP1 that the relative amount of hematite increases only gradually with each additional P25 loading in magnetic P25 (FPx) particles. This shows that the surface coverage of the magnetic particle with P25 is almost complete at the 1:1 mass loading ratio.

An estimate of the relative loading of P25 on the magnetic particles is obtained from the XRD patterns shown in Fig. 3. Here the P25 peaks clearly increase in intensity relative to the iron oxide peaks with high P25 loading. The ratio of the  $\text{TiO}_2$  (1 0 1) peak at  $25.3^\circ$  to the total iron oxide (1 1 0) peak at  $35.6^\circ$  is linear with the starting mass ratio of up to FP5 (Fig. S3). The small increase in magnetite to hematite conversion above FP1, coupled with the linear increase in P25 loading, shows that the thickness of the P25 coating increasing with P25 loading up to FP5 (Fig. S3).

The XRD patterns for the magnetic particles before and after coating with  $\text{SiO}_2$  are shown in Fig. 4a and b, respectively. All peaks for the magnetic particles in Fig. 4a and b are assigned to magnetite and show that these particles remain unchanged after coating with  $\text{SiO}_2$ . This is expected, given the amorphous structure of the  $\text{SiO}_2$  sol-gel coating and that the coating procedure was performed at room temperature. After calcination (Fig. 4c), weak peaks at  $23.8^\circ$  and  $26.1^\circ$  show that a small amount of the magnetite is converted to maghemite. There is little oxidation of the magnetic particles, which is in contrast to what occurs upon calcination of bare magnetite particles or the FPx samples. In essence, the  $\text{SiO}_2$  layer encapsulates the magnetic particles and inhibits reaction with the oxygen in the air.

Fig. 4d is the XRD pattern for FSP2. There are small peaks due to maghemite, but no peaks due to hematite; thus, the  $\text{SiO}_2$  layer inhibits the redox reaction of the magnetite core with P25, since P25 is not in direct contact with the underlying magnetite particles. It is noted that after rinsing the FSP2 samples in water, the water turns into a white cloudy solution, indicating that some P25 is removed during this step. This is confirmed from the XRD data. The peak intensity ratio of  $25.3^\circ:35.6^\circ$  for FSP2 (Fig. 4d) shows that the P25 around the magnetic particles is 50% of that obtained for FP2 (Fig. 3c). This shows that P25 does not adsorb strongly to  $\text{SiO}_2$ -coated magnetic particles. Recall that the samples FPx ( $x < 3$ ) show a linear growth with P25 loading (Fig. S3) and in this case, a clear solution phase was obtained after the rinsing step.

To securely anchor the P25 on top of the silica coating, we introduced a second  $\text{TiO}_2$  sol-gel layer. It has been reported that covalent Si-O-Ti linkages form between the  $\text{SiO}_2$  and  $\text{TiO}_2$  layer leading to a strongly bound  $\text{TiO}_2$  layer on the  $\text{SiO}_2$  [28]. Fig. 4e shows the XRD

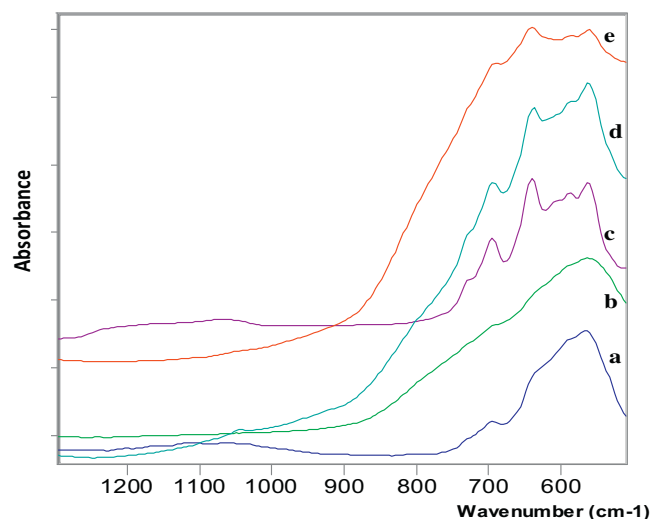


**Fig. 5.** IR spectra of (a) calcined magnetite particles (b) FP1, (c) FS calcined, (d) FST, and (e) FSTP1.

pattern for a FST sample. The weak broad (1 0 1) peak of  $\text{TiO}_2$  at  $25.3^\circ$  is observed due to a  $\text{TiO}_2$  thin layer around the magnetic particles. There are no hematite peaks after calcination because of the presence of the  $\text{SiO}_2$  barrier. The FST particles are then calcined with the P25 paste to obtain the FSTPx particles. Fig. 4f and g are XRD patterns for FSTP1 and FSTP2, respectively, and show that the ratio of P25 to magnetite for FSTP1 and FSTP2 samples are the same as the corresponding FPx sample (Fig. 3b, c). Higher loadings of P25 were prepared (eg., FSTPx,  $x = 3, 4, 5$ ) but these samples showed loss of P25 during the rinse step.

Elemental analysis using the ICPMS for synthesized samples showed agreement with XRD results in the total amount of Fe and Ti in the samples. XRD data show that the amounts of  $\text{TiO}_2$  and magnetic particles in the synthesized particles are within about  $\pm 10\%$  of those determined by the ICPMS and the starting mass formulation. ICPMS was also conducted to measure the presence of dissolution products in the solution after UV illumination experiments. In all cases, the photodissolution of Ti, Si, and Fe into solution was found negligible at 0.005–0.04 mg/L, which translates to about 0.001–0.03% of the total mass of each sample (Table S3).

### 3.2. FT-IR analysis

Evidence of covalently attached  $\text{SiO}_2$  and  $\text{TiO}_2$  layers is provided by IR spectral analysis. The IR spectrum of the calcined magnetic particles (Fig. 5a) shows a broad Fe-O bulk mode near  $560\text{ cm}^{-1}$  [47]. Fig. 5b is the spectrum for FP1, where the peak at  $560\text{ cm}^{-1}$  is broader to the high wavenumber side, due to the presence of the Ti-O bulk mode of P25. The spectrum of sample FS (Fig. 5c) has a broad band at  $1093\text{ cm}^{-1}$  due to a Si-O-Si bulk mode. Several bands in the  $650\text{--}600\text{ cm}^{-1}$  are assigned to the Si-O-Fe mode and provide evidence of a covalently attached silica layer. For sample FST (Fig. 5d), there is a tail on the high wavenumber side on the broad band at  $600\text{ cm}^{-1}$  showing the presence of a  $\text{TiO}_2$  coating. This Ti-O mode is more intense in the spectrum for sample FSTP1 (Fig. 5e) due to the additional P25 on the surface.

### 3.3. XPS analysis

Fig. 6 shows the XPS spectrum for FP1. Peaks for aluminum and carbon are from the substrate used for holding the powder samples. Peaks due to Ti and O are obtained, along with a weak Fe peak that could be either due to incomplete surface coverage or diffusion of Fe

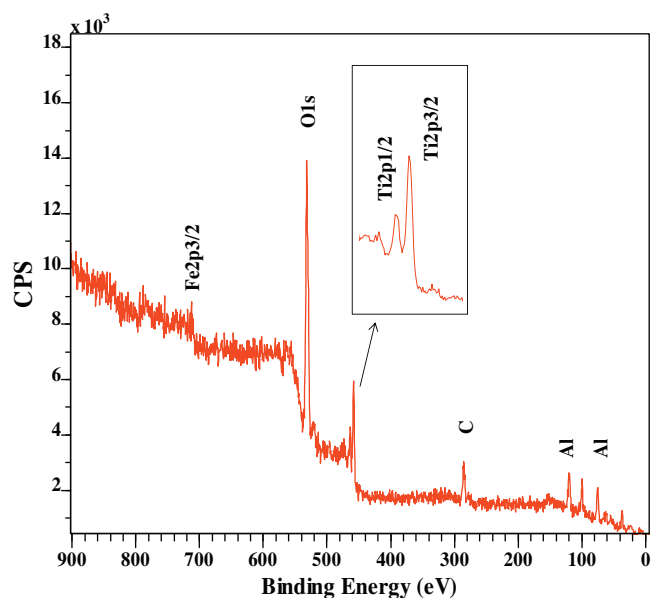


Fig. 6. XPS spectra for the FP1.

**Table 2**  
Binding energy for Ti 2p<sub>3/2</sub> and O1s.

Samples	Ti 2p <sub>3/2</sub> (eV)	O1s (eV)
P25	460.5	532
FP1	458.0	532
FP2	457.4	532
FSTP1	459.2	532
FSTP2	459.4	532

from the core to the P25 surface [37]. However, for sample FP2, no Fe peak is observed (Fig. S5). Therefore, it is likely that the Fe peak obtained in the XPS spectrum of FP1 is due to incomplete coverage and not diffusion of Fe from the core. XPS spectra for other samples are shown in the SI section (Fig. S5–S8). In these spectra, there is no Fe peak which indicates that the average thickness of the P25 layer is >10 nm.

Table 2 shows the binding energy for the Ti2p<sub>3/2</sub> and O1s peaks for pure P25 and the various coated magnetic particles. The binding energy for the Ti 2p<sub>3/2</sub> peak is 460.5 eV for pure P25. For samples FP1 and FP2, this binding energy shifts to lower energies, consistent with the Ti being reduced which provides additional evidence of a redox reaction between P25 and the magnetite particles. For samples FSTP1 and FSTP2, the Ti2p<sub>3/2</sub> binding energies are lower than that for pure P25 and higher than that for FPx. However, the XRD spectra show no conversion of magnetite to hematite and thus, there is no reduction of the P25 in FSTPx particles to account for the shift in binding energy. This shift in binding energy may arise from direct contact of the TiO<sub>2</sub> with the SiO<sub>2</sub> layer [48]. Silica is more electronegative than Ti and the substitution of Ti atoms by Si in the Si–O–Ti bond decreases the coordination number around Ti and leads to a shift in the Ti2p<sub>3/2</sub> binding energy.

### 3.4. TEM analysis

The TEM images of bare magnetite particles and FP2 are shown in Fig. 7a and b, respectively. The TEM in Fig. 7b shows magnetite particles coated with clusters of P25. A TEM image of a single particle of SiO<sub>2</sub>-coated magnetic particles (FS) in Fig. 7c shows a thin layer of silica of a non-uniform thickness around the particle (~10–15 nm), which is in agreement with the XPS data.

**Table 3**

Specific surface area of Pure P25 and coated magnetic particles.

Photocatalyst	Specific surface area (m <sup>2</sup> g <sup>−1</sup> )	Estimated specific surface area normalized with respect to P25 (m <sup>2</sup> g <sup>−1</sup> )
P25	59 (±0.5)	59
FP1	31 (±0.1)	62
FP2	41 (±0.2)	62
FP3	44 (±0.2)	58
FST	70 (±0.2)	–
FSTP1	53 (±0.3)	36
FSTP2	61 (±0.2)	56
F <sub>3</sub> O <sub>4</sub>	9.5 (±0.1)	–

Fig. 7d is the TEM image of a single particle of FST, and Fig. 7e and f are TEM images of FSTPx. The TEM image of the FST single particle in Fig. 7d shows a non-uniform TiO<sub>2</sub> layer on top of the silica coating. The TiO<sub>2</sub> sol-gel layer around the sample FST is thinner than the P25 layer for samples FSTPx, as shown in Fig. 7e and f. This is consistent with the XRD data (Fig. 4e) which shows that the TiO<sub>2</sub> peak intensity in FST particles is less than 5% of TiO<sub>2</sub> peak intensity in FSTP1 particles. The thickness of the P25 layer around the magnetic particles shown by the TEM image in Fig. 7f is not uniform and varies in the range of 20–100 nm. Furthermore, the P25 primary particles are in the form of clusters on the surface. It is noted that P25 does not exist as primary particles but rather as a cluster of primary particles of about 0.2 μm diameter. This is true for all fumed particles such as silica, titania and alumina. This is due to sintering between particles that occurs during the transition from the high temperature of synthesis and the cooling down process. These clustered aggregates cannot be broken down into smaller particles by physical processing. In addition these aggregates can cluster into larger loosely associated agglomerates in solution. We observe the same clusters of aggregates of P25 deposited on the magnetic particles.

Based on the SEM images (Fig. S9) and EDX data (Table S5), the Fe:Ti ratios are not uniformly distributed on the particle surfaces. Again this is consistent with the adsorption of P25 aggregates. However, EDX analysis showed the presence of Ti with Fe in every sample supporting the XPS data that Ti surface coverage is complete and > 10 nm.

### 3.5. Surface area measurements

Table 3 shows the specific surface areas of coated magnetic particles obtained from BET analysis. For FPx particles, (x = 1–3), the surface areas increase with the relative amount of P25. However, the measured specific surface areas also include mass from the magnetic core and thus, underestimates the specific surface area of the P25. In the second column of Table 3, we have subtracted the mass of the magnetic particles from the overall mass, assuming that the starting formulation mass ratio of magnetic particles to P25 is conserved in the final particles. This assumption is reasonable given that the XRD and ICPMS data (Tables S2 and S4) shows that the amount of TiO<sub>2</sub> and magnetic particles in the synthesized samples are within ±10% of the starting formulation. For the FPx samples, after subtracting the mass contribution of the magnetic core from the total mass, all samples show similar surface area with pure P25. This again is reasonable given the adsorption of P25 aggregates on the surface. Thus, the elevated temperature sintering of the P25 to the magnetic core is not accompanied with any appreciable loss in surface area of the P25 particles.

The FST surface area of 70 m<sup>2</sup> g<sup>−1</sup> is significantly higher than the 9.5 m<sup>2</sup> g<sup>−1</sup> measured for the magnetic particles. Thus, for the FST sample, simple subtraction of the mass of the core when determining the surface area of the P25 is not valid. When the FST samples are coated with P25 particles, the surface area decreases from 70

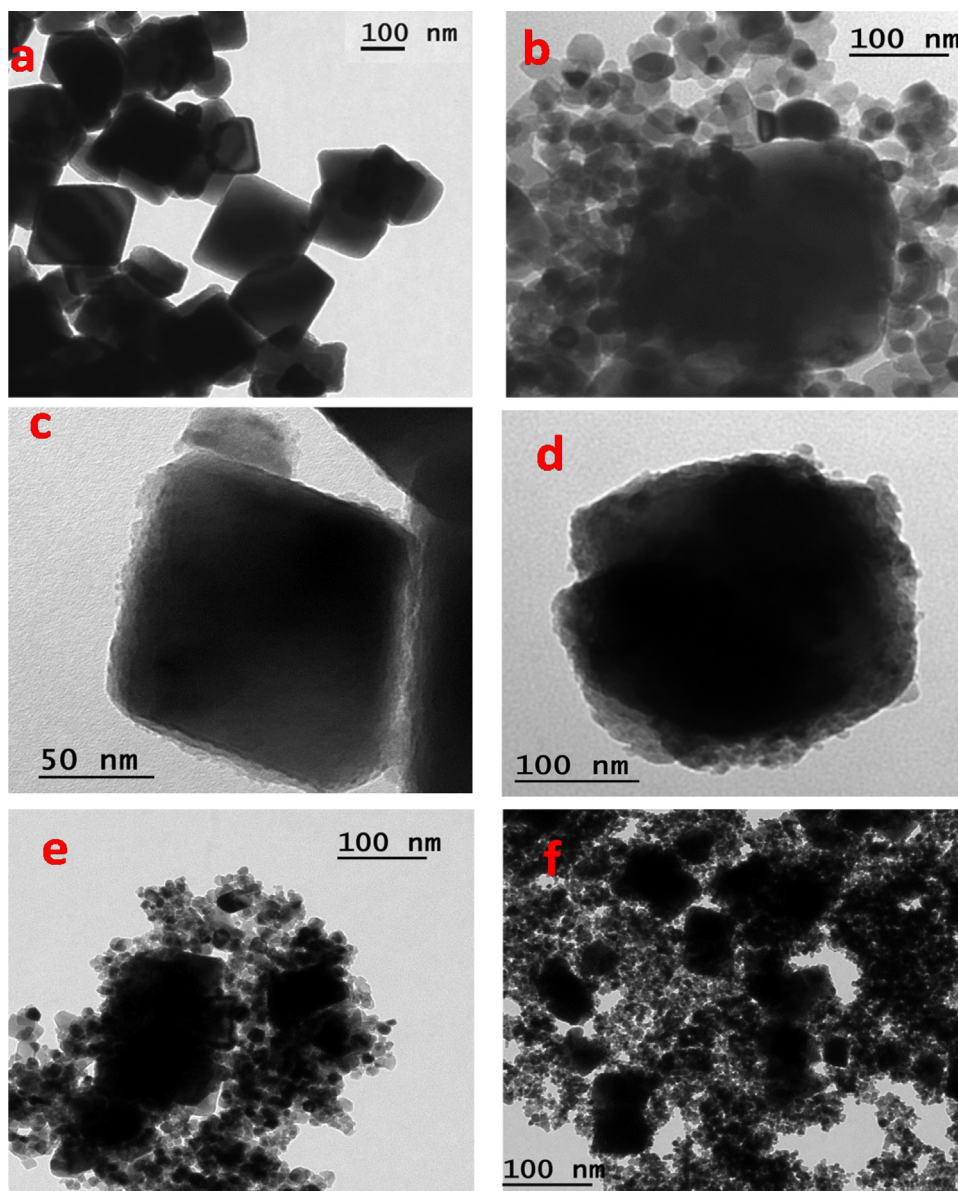


Fig. 7. TEM images of (a) magnetite, (b) FP2, (c) FS, (d) FST, (e) FSTP1, and (f) FSTP2.

to 53 and  $61 \text{ m}^2 \text{ g}^{-1}$  for FSTP1 and FSTP2, respectively. A drop in surface area is expected because P25 particles have a lower surface area ( $59 \text{ m}^2 \text{ g}^{-1}$ ) than the underlying FST ( $70 \text{ m}^2 \text{ g}^{-1}$ ). The TEM images of FSTP1 and FSTP2 particles (Fig. 7e and f) show that the P25 is a thick but loosely sintered cluster of P25 primary particles around a magnetic core. Thus, we assume that there would be little change in the surface area of the underlying FST surface with P25 loading. In this case, the overall measured surface area would be,

$$SA_{FSTPx} = \frac{(SA_{FST} * FSTmass) + (X * P25mass)}{Totalmass} \quad (1)$$

where  $SA$  = surface area ( $\text{m}^2 \text{ g}^{-1}$ ), and  $x$  = calculated  $SA$  of the P25 layer in the FSTPx sample.

Using Eq. (1), we calculate a surface area of  $56 \text{ m}^2 \text{ g}^{-1}$  for the P25 layer in sample FSTP2, which is close to  $59 \text{ m}^2 \text{ g}^{-1}$  measured for P25 particles. Thus, we conclude that there is insignificant reduction in surface area of the P25 coating in the FSTP2 sample. Details of the surface area calculations are provided in the SI section.

### 3.6. Magnetic properties of photocatalyst

As shown in Fig. 8, pure magnetite, FSTP2, and FP2 have magnetization saturation ( $M_s$ ) values of 77, 40, and  $10 \text{ emu g}^{-1}$ , respectively. The  $M_s$  value for bare iron oxide magnetic particles is similar to values reported in the literature [30,31]. The conversion of magnetite to hematite in FP2 is consistent with the observed magnetization decrease to  $10 \text{ emu g}^{-1}$ . In contrast, FSTP2 exhibits  $M_s$  value higher than FP2 but still lower than the bare magnetite, which is attributed to magnetization screening provided by the thick layer of P25 on the surface of magnetite.

### 3.7. Photocatalytic activity

The photogenerated electron-hole pair in the coated magnetic particles decomposes water to produce  $\text{HO}^\bullet$  that was monitored by hTPA formation. At the  $83 \text{ mg/L}$  initial concentration of TPA used in this work, the generated hTPA reaches concentrations that are sufficient to result in self quenching, leading to nonlinearity in the fluorescence intensity with respect to hTPA concentration.

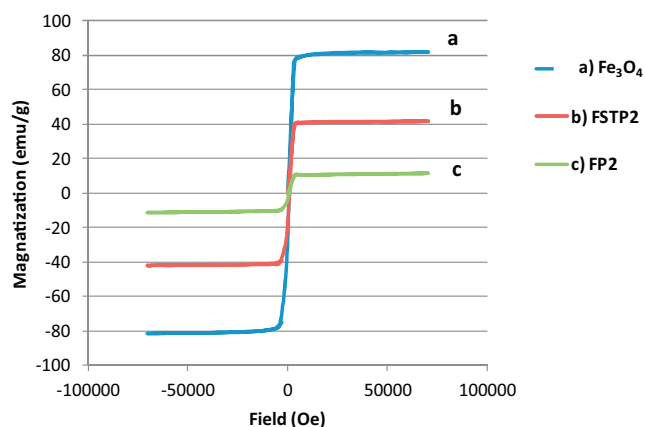


Fig. 8. The room-temperature magnetization curves of (a) magnetite, (b) FSTP2, and (c) FP2.

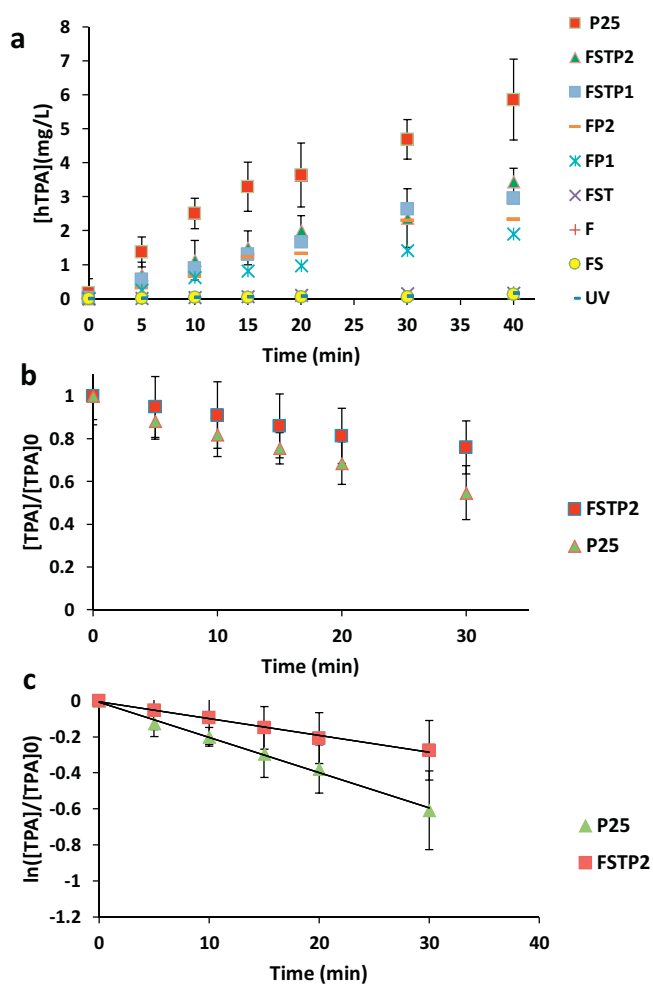


Fig. 9. (a) hTPA concentration versus UV radiation time for all photocatalyst (0.5 g/L), (b) TPA relative concentration versus UV irradiation time, and (c) TPA degradation rate (initial TPA concentration = 83 mg/L and all photocatalysts concentration = 0.5 g/L).

At a twenty-fold dilution of hTPA, self quenching is not observed and a linear relationship exists between hTPA concentration and fluorescence intensity.

Fig. 9a shows the hTPA concentration versus irradiation time for each sample. In all cases, the hTPA formation is linear with respect to time [49–52]. In several control experiments (i.e., UV irradiation

of the TPA solution containing no particles, bare magnetic particles, or FS particles) there was negligible reaction, showing that UV irradiations under conditions of no P25 present does not produce  $\text{HO}^\bullet$ .

A stated goal of this work was to produce a photocatalyst with magnetic properties that had equal photocatalytic degradation rates to that of P25 particles. Yu et. al. [7], reported photocatalytic degradation rates for sol-gel  $\text{TiO}_2$ - and  $\text{SiO}_2$ -coated magnetic particles (similar to FST particles in this study) equivalent to that of P25. Our experiments showed that the activity of our FST particles with respect to  $\text{HO}^\bullet$  production was 5% of P25 particles, which is just above what was obtained for UV illumination without any photocatalyst present (Fig. 9a). In contrast, the P25-coated particles (i.e., FPx and FSTPx) had higher photocatalytic rates, with FSTPx particles showing more activity compared to FPx particles. The higher activity in FSTPx is most likely due to the insulative effect of  $\text{SiO}_2$  coatings.

The initial photocatalytic degradation of TPA follows pseudo first-order kinetics [51,52] and the formation of hTPA follows pseudo zero-order kinetics [43,49,51–53]. From this, the initial rate constants for hTPA, and hence  $\text{HO}^\bullet$ , formation by P25 and FSTP2 are  $0.234 \pm 0.177$  and  $0.112 \pm 0.051 \text{ M min}^{-1}$ , respectively on a total mass of catalyst basis (Fig. 9a). The FSTP2 samples tested with the same particles twice resulted in the same OH radical yield. Dark adsorption was minimal ( $\sim 3.0\%$ ) for TPA and phenol on both P25 and FSTP2 after a 15 min incubation and this value did not change after a 30 min stirring. Fig. 9b shows TPA photocatalytic degradation versus irradiation time using P25 and FSTP2 catalysts. After a 30 min reaction time, 38% of the TPA is decomposed by P25 compared to 20% for FSTP2. Using pseudo-first order reaction kinetics for TPA photocatalytic degradation [36,54], rate constants (Fig. 9c) for TPA photocatalytic degradation by P25 and FSTP2 are  $0.0152 \pm 0.003$  and  $0.0146 \pm 0.005 \text{ min}^{-1}$ , respectively.

The photocatalytic degradation of phenol by P25 and FSTP2 particles were also studied (Fig. 10a). After 30 min of irradiation, more than 97% and 88% of phenol is degraded by P25 and FSTP2, respectively. Photocatalytic degradation of phenol follows first order reaction kinetics [42,55], and the corresponding first-order rate constants by P25 and FSTP2 are  $0.087 \pm 0.02$  and  $0.067 \pm 0.03 \text{ min}^{-1}$ , respectively (Fig. 10b).

It is noted that we have reported decomposition based on total mass of the photocatalyst and that a significant fraction of this mass comes for the magnetic core. When we calculate the rates on a per P25 mass, instead of total mass, the rates between P25 and FSTP2 are similar. The values obtained for TPA photocatalytic degradation are  $0.0152 \pm 0.003 \text{ min}^{-1}$  for P25 and  $0.0144 \pm 0.007 \text{ min}^{-1}$  for FSTP2. These rate constants for phenol photocatalytic degradation are  $0.09 \pm 0.02 \text{ min}^{-1}$  for P25 and  $0.10 \pm 0.04 \text{ min}^{-1}$  for FSTP2. Since the effective surface area of the P25 aggregates on the magnetic particles is similar to P25 suspensions it is reasonable that the P25 aggregates in the solution would have similar mass transport behavior as the same aggregates deposited on the magnetic particles. This results in similar rate constants based on amount of P25 on the coated magnetic particles and P25 for the photocatalytic degradation of TPA and phenol. We note that there could be differences in the level of illumination for magnetic particles and P25 suspension and the impact of this on the measured rate constants are not known.

#### 4. Conclusions

The key development of this study was to use underlying  $\text{SiO}_2$  layer coating magnetite particles followed by a  $\text{TiO}_2$  layer applied, using the sol-gel technique, to effectively anchor the P25 to the particles. This resulted in a 1:2 mass ratio of P25 to the magnetic

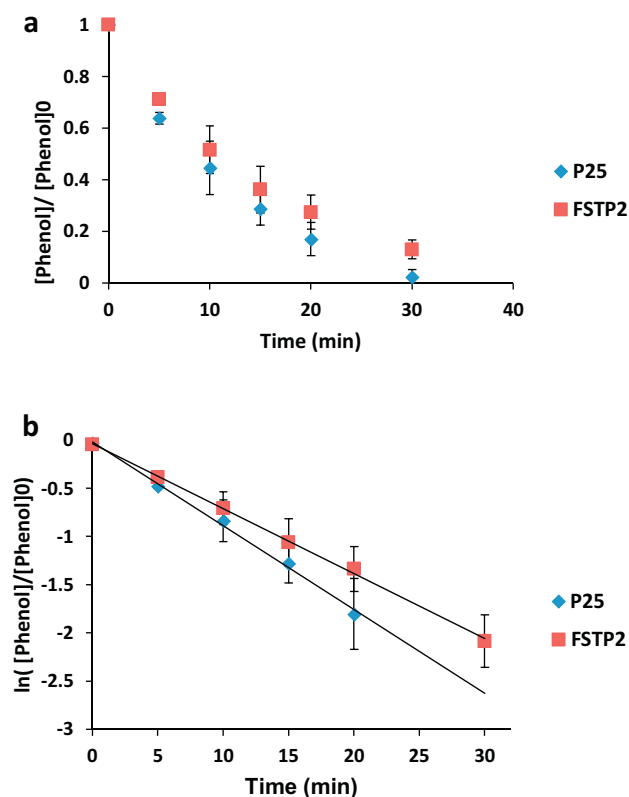


**Fig. 10.** (a) Phenol relative concentration versus UV irradiation time, and (b) phenol degradation rate (initial phenol concentration = 10 mg/L and all photocatalysts concentration = 0.5 g/L).

particles. These sol-gel TiO<sub>2</sub>- and SiO<sub>2</sub>-coated P25 magnetic particles displayed equivalent photocatalytic degradation rates as P25 based on experimental data for TPA and phenol. When compared on a mass of P25 basis, coated magnetic particles produced similar decomposition rates which was attributed to the similar surface area of the P25 in both cases. In the absence of any SiO<sub>2</sub> coating, the P25 adsorbed strongly to the magnetic particles through a redox reaction, but the coated particles exhibited lower HO<sup>•</sup> production rates compared to P25 alone.

The magnetic photocatalyst particles produced here can be used for water and wastewater treatment. The nano-particle nature of these particles facilitates mass transfer of contaminants to the reactive surface sites, and their magnetic character allows their downstream separation and recycling back into the irradiation chamber. Future research should address the efficacy of the magnetic photocatalysts with respect to different classes of organic contaminants, such as pharmaceutical and personal care products, algal toxins, and byproducts of chlorine disinfection, as well as microorganisms, such as viruses and bacteria in water. Given the effectiveness of UV irradiation at 254 nm with respect to inactivation of microorganisms [56], further research needs to be conducted to show the effect of the magnetic photocatalysts on this germicidal activity.

## Acknowledgments

The authors thank Dr. R. J. Lad, Dr. D. Frankel, Dr. G. Bernhardt from the Laboratory for Surface Science and Technology (LASST), University of Maine for help with performing the SEM, XRD and XPS measurements and for help with interpreting the spectra. Dr. B. Frederick is acknowledged for his help in providing BET (N<sub>2</sub>) data. Dr. B. Cole and Mr. D. LaBrecque are also acknowledged for

their help in performing fluorescence and HPLC measurements. Partial funding for this work was provided by the USGS-WRRI Grant Program.

## Appendix A. Supplementary data

Supplementary data associated with this article can be found, in the online version, at <http://dx.doi.org/10.1016/j.apcatb.2016.01.008>.

## References

- [1] R.R. Trussell, D.W. Hand, MWH's Water Treatment Principles and Design, 3rd edition, John Wiley & Sons Hoboken, NJ, USA, 2012.
- [2] M.T. Amin, A.A. Alazba, U. Manzoor, Adv. Mater. Sci. Eng. 2014 (2014) 24.
- [3] A.C. Eiseheid, J.A. Thurston, K.G. Linden, Crit. Rev. Environ. Sci. Technol. 41 (2011) 1375–1396.
- [4] M.R. Hoffmann, S.T. Martin, W. Choi, D.W. Bahnemann, Chem. Rev. 95 (1995) 69–96.
- [5] M. Antonopoulou, E. Evgenidou, D. Lambropoulou, I. Konstantinou, Water Res. 53 (2014) 215–234.
- [6] C. McCullagh, J.C. Robertson, D. Bahnemann, P.J. Robertson, Res. Chem. Intermed. 33 (2007) 359–375.
- [7] X. Yu, S. Liu, J. Yu, Appl. Catal. B: Environ. 104 (2011) 12–20.
- [8] R. Wang, X. Wang, X. Xi, R. Hu, G. Jiang, Adv. Mater. Sci. Eng. 2012 (2012) 8.
- [9] B. Ohtani, O.O. Prieto-Mahaney, D. Li, R. Abe, J. Photochem. Photobiol. A: Chem. 216 (2010) 179–182.
- [10] D.C. Hurum, K.A. Gray, T. Rajh, M.C. Thurnauer, J. Phys. Chem. B 109 (2005) 977–980.
- [11] D.O. Scanlon, C.W. Dunnill, J. Buckeridge, S.A. Shevlin, A.J. Logsdail, S.M. Woodley, C.R.A. Catlow, M.J. Powell, R.G. Palgrave, I.P. Parkin, G.W. Watson, T.W. Keal, P. Sherwood, A. Walsh, A.A. Sokol, Nat. Mater. 12 (2013) 798–801.
- [12] A.Y. Shan, T.I.M. Ghazi, S.A. Rashid, Appl. Catal. A: Gen. 389 (2010) 1–8.
- [13] H. Yoneyama, S. Haga, S. Yamanaka, J. Phys. Chem. 93 (1989) 4833–4837.
- [14] J. Sabate, M.A. Anderson, H. Kikkawa, M. Edwards, C.G. Hill Jr., J. Catal. 127 (1991) 167–177.
- [15] W. Su, T. Zhang, L. Li, J. Xing, M. He, Y. Zhong, Z. Li, RSC Adv. 4 (2014) 8901–8906.
- [16] H. Niu, Q. Wang, H. Liang, M. Chen, C. Mao, J. Song, S. Zhang, Y. Gao, C. Chen, Materials 7 (2014) 4034–4044.
- [17] W.-F. Ma, Y. Zhang, L.-L. Li, L.-J. You, P. Zhang, Y.-T. Zhang, J.-M. Li, M. Yu, J. Guo, H.-J. Lu, C.-C. Wang, ACS Nano 6 (2012) 3179–3188.
- [18] U. Sirimahachai, N. Ndiege, R. Chandrasekharan, S. Wongnawa, M. Shannon, J. Sol-Gel Sci. Technol. 56 (2010) 53–60.
- [19] M.J.G. Salazar, Development and Application of Titanium Dioxide Coated Magnetic Particles for Photocatalytic Oxidation of Aqueous Phase Organic Pollutants, der Technischen Universität Berlin, Berlin, 2010, pp. 121.
- [20] R. Bangxing, H. Changseok, H.A.A. Abdulaziz, N.N. Mallikarjuna, D.D. Dionysios, Interactions of nanomaterials with emerging environmental contaminants, Am. Chem. Soc. (2013) 135–146.
- [21] J. Zhan, H. Zhang, G. Zhu, Ceram. Int. 40 (2014) 8547–8559.
- [22] D. Beydoun, R. Amal, G.K.C. Low, S. McEvoy, J. Phys. Chem. B 104 (2000) 4387–4396.
- [23] C.-T. Chen, Y.-C. Chen, Anal. Chem. 77 (2005) 5912–5919.
- [24] Z. Teng, X. Su, G. Chen, C. Tian, H. Li, L. Ai, G. Lu, Colloids Surf. A: Physicochem. Eng. Asp. 402 (2012) 60–65.
- [25] J. Li, L. Gao, Q. Zhang, R. Feng, H. Xu, J. Wang, D. Sun, C. Xue, J. Nanomater. 2014 (2014) 7.
- [26] S. Tawkaew, S. Supothina, Mater. Chem. Phys. 108 (2008) 147–153.
- [27] F. Chen, Y.D. Xie, J.C. Zhao, G.X. Lu, Chemosphere 44 (2001) 1159–1168.
- [28] F. Chen, J. Zhao, Catal. Lett. 58 (1999) 246–247.
- [29] Y. Li, J. Wu, D. Qi, X. Xu, C. Deng, P. Yang, X. Zhang, Chem. Commun. (2008) 564–566.
- [30] M. Abbas, B.P. Rao, V. Reddy, C. Kim, Ceram. Int. 40 (2014) 11177–11186.
- [31] Y. Chi, Q. Yuan, Y. Li, L. Zhao, N. Li, X. Li, W. Yan, J. Hazard. Mater. 262 (2013) 404–411.
- [32] K. Hofstadler, R. Bauer, S. Novalic, G. Heisler, Environ. Sci. Technol. 28 (1994) 670–674.
- [33] A. Hasanpour, M. Niyaifar, H. Mohammadpour, J. Amighian, J. Phys. Chem. Solids 73 (2012) 1066–1070.
- [34] M. Niyaifar, A. Hasanpour, H. Mohammadpour, J. Amighian, Phys. Status Solidi (a) 210 (2013) 1190–1194.
- [35] M.S.T. Goncalves, A.M.F. Oliveira-Campos, E.M.M.S. Pinto, P.M.S. Plasencia, M.J.R.P. Queiroz, Chemosphere 39 (1999) 781–786.
- [36] A. Shafaei, M. Nikazar, M. Arami, Desalination 252 (2010) 8–16.
- [37] Y. Chen, D.D. Dionysiou, Appl. Catal. B: Environ. 62 (2006) 255–264.
- [38] Y. Chen, D.D. Dionysiou, Appl. Catal. A: Gen. 317 (2007) 129–137.
- [39] G. Balasubramanian, D.D. Dionysiou, M.T. Suidan, I. Baudin, J.-M. LaA±ñA©, Appl. Catal. B: Environ. 47 (2004) 73–84.
- [40] G. Balasubramanian, D.D. Dionysiou, M.T. Suidan, V. Subramanian, I. Baudin, J.M. Laine, J. Mater. Sci. 38 (2003) 823–831.
- [41] S.E. Page, W.A. Arnold, K. McNeill, J. Environ. Monit. 12 (2010) 1658–1665.

- [42] J. Ryu, W. Choi, *Environ. Sci. Technol.* 42 (2008) 294–300.
- [43] K.-I. Ishibashi, A. Fujishima, T. Watanabe, K. Hashimoto, *Electrochem. Commun.* 2 (2000) 207–210.
- [44] C.G. Hatchard, C.A. Parker, *Proc. R. Soc. Lond. Ser. A Math. Phys. Sci.* 235 (1956) 518–536.
- [45] Z. Pan, E.A. Stemmler, H.J. Cho, W. Fan, L.A. LeBlanc, H.H. Patterson, A. Amirbahman, *J. Hazard. Mater.* 279 (2014) 17–25.
- [46] J.-Y. Shin, J.H. Joo, D. Samuelis, J. Maier, *Chem. Mater.* 24 (2012) 543–551.
- [47] A.L. Andrade, D.M. Souza, M.C. Pereira, J.D. Fabris, R.Z. Domingues, *Cerâmica* 55 (2009) 420–424.
- [48] H. Cao, P. Du, L. Song, J. Xiong, J. Yang, T. Xing, X. Liu, R. Wu, M. Wang, X. Shao, *Mater. Res. Bull.* 48 (2013) 4673–4678.
- [49] J. Yu, W. Wang, B. Cheng, B.-L. Su, *J. Phys. Chem. C* 113 (2009) 6743–6750.
- [50] B. Tryba, M. Toyoda, A.W. Morawski, R. Nonaka, M. Inagaki, *Appl. Catal. B: Environ.* 71 (2007) 163–168.
- [51] U. Černigoj, M. Kete, U.L. Stangar, *Catal. Today* 151 (2010) 46–52.
- [52] M. Kete, E. Pavlica, F. Fresno, G. Bratina, U.L. Stangar, *Environ. Sci. Pollut. Res.* 21 (2014) 11238–11249.
- [53] Q. Xiao, Z. Si, J. Zhang, C. Xiao, X. Tan, *J. Hazard. Mater.* 150 (2008) 62–67.
- [54] R. Thiruvengkatachari, T.O. Kwon, J.C. Jun, S. Balaji, M. Matheswaran, I.S. Moon, *J. Hazard. Mater.* 142 (2007) 308–314.
- [55] B. Tryba, A.W. Morawski, M. Inagaki, M. Toyoda, *Appl. Catal. B: Environ.* 63 (2006) 215–221.
- [56] K. Linden, G. Shin, Sobsey, *Water Sci. Technol.* 43 (2001) 171.